Citation for published version

Gu, Chao and Gao, Steven and Fusco, Vincent and Gibbons, Gregory and Sanz-Izquierdo, Benito and Standaert, Alexander and Reynaert, Patrick and Bösch, Wolfgang and Gadringer, Michael and Xu, Rui and Yang, Xuexia (2020) A D-band 3D printed antenna. IEEE Transactions on Terahertz Science and Technology . ISSN 0018-926X.

DOI

https://doi.org/10.1109/TTHZ.2020.2986650

Link to record in KAR

https://kar.kent.ac.uk/81234/

Document Version

Author's Accepted Manuscript

A D-band 3D-Printed Antenna

Chao Gu, Steven Gao, *Fellow, IEEE*, Vincent Fusco, *Fellow, IEEE*, Gregory Gibbons, Benito Sanz-Izquierdo, Alexander Standaert, Patrick Reynaert, *Senior Member, IEEE*, Wolfgang Bösch, *Fellow, IEEE*, Michael Gadringer, Rui Xu, Xuexia Yang

Abstract— **This paper reports the design and fabrication of a novel all-metal antenna operating in the millimeter-wave band. Based on the resonant cavity antenna (RCA) concept, the principle of antenna operation is explained, and parametric studies of several key design parameters are provided. A novel impedance matching technique is introduced to broaden the antenna return loss bandwidth. Two gain enhancement methods have been employed to achieve a more directive beam with reduced side lobes and back lobes. The D-band antenna prototypes are produced using i) all-metal printing without any postprocessing; ii) dielectric printing with copper metallization applied later. Comparisons of the simulated and measured results amongst the antennas fabricated using the two additive manufacturing techniques are made. Measurement results of the two antenna prototypes show that the proposed design can achieve a 14.2% bandwidth with a maximum gain of 15.5 dBi at 135 GHz. The present work is the first D-band resonant cavity antenna fabricated using two different 3D printing methods.**

Index Terms—**D-band, low THz, 3D printing, additive manufacturing, waveguide feed, resonant cavity antenna, all-metal.**

I. INTRODUCTION

MILLIMETER-WAVE (mmW) and submillimeter-wave technologies are finding new applications for commercial development in recent years [1]. Rapid progress has been made to develop industrial fabrication and integration of millimeter-wave systems operating from 100 GHz to 300 GHz. As such, these bands are of great potential to be implemented in a range of promising applications in the near future. For example, the sixth-generation wireless mobile communication is expected to enable ultrafast connectivity, targeting at a maximum data rate of 100 Gbit/s around 300 GHz [2]. The implementation of electronic devices and integrated circuits at mmW and sub-mmW frequencies requires suitable and robust packaging to meet the requirement of the signal loss, dimension, and fabrication issues for practical applications [3]. In this context, the antenna development needs to be carefully carried out considering packaging cost and performance in the bands above 100 GHz. Two major packaging technologies have been employed in mmW and sub-mmW systems. One approach is the quasi-optical packaging, where dielectric lenses are mounted in front of on-chip antennas [4], [5]. The planar antennas can be designed and fabricated along with monolithic microwave integrated circuits (MMIC) to avoid the interconnection loss and prevent circuit parasitic effects and fabrication tolerances. Non-conductive epoxy glue is used to attach the lens with the on-chip radiator. Here, accurate alignment is required to ensure the feed point is located at the focal point of the lens; otherwise, the beam peak will shift off the boresight direction [6]. Another packaging method is to use split waveguide blocks. Waveguide interfaces are the most commonly used at mmW through sub-mmW bands due to the low loss and high-power capacity. From the measurement perspective, the measurement setup for characterizing waveguide fed antennas can be easier than the on-wafer measurement of the on-chip antennas. Recently, transitions can be integrated with the bare die with an insertion loss as low as 1 dB at 500 GHz [7], which enables easy and cost-effective coupling to external waveguide fed antennas. Thus, horns, reflectors, and lenses can be employed as the transmit/receive antennas to form directive beams. Generally, these antennas require high-precision computer numerical control (CNC) milling to ensure high surface accuracy and low surface roughness. Due to the increasingly small antenna structures imposed by the wavelengths of operation, the antenna fabrication becomes difficult, costly, and time-consuming. To tackle the challenges and further explore waveguide fed antenna solutions, several antenna designs with different fabrication processes have been developed to operate above 100 GHz. Silicon-based micromachining technologies have enabled 3-D antennas, e.g., corrugated horn, silicon lens, for operations up to 1.9 THz with the maximum aperture efficiency of 85% [8]-[10]. Authors in [11] propose a substrate integrated waveguide fed slot antenna array that can be fabricated using low-temperature co-fired ceramic (LTCC) technology. Operating at 140 GHz, the antenna achieves a maximum measured gain and efficiency of 21.3 dBi and 34 %, respectively. Although LTCC technology offers reliable assembly and packaging of front-end components in a single

---

Manuscript received xx, xx, 2020.

C. Gu and V. Fusco are with Institute of Electronics, Communications & Information Technology, Queen's University Belfast, UK (e-mail: chao.gu@qub.ac.uk).

S. Gao, B. Sanz, and R. Xu are with School of Engineering and Digital Arts, University of Kent, Canterbury, UK.

A. Standaert and P. Reynaert are with the MICAS Division, Department of Electrical Engineering (ESAT), Katholieke Universiteit Leuven, 3000 Leuven, Belgium.

G. Gibbons is with Warwick Manufacturing Group, University of Warwick, Coventry, UK

M. Gadringer and W. Bosch are with Microwave and Photonic Engineering, Graz University of Technology, Graz, Austria.

X. Yang is with School of Communication and Information Engineering, Shanghai University.

This article has been accepted for publication in a future issue of this journal, but has not been fully edited. Content may change prior to final publication. Citation information: DOI 10.1109/TTHZ.2020.2986650, IEEE Transactions on Terahertz Science and Technology

multilayer laminated package, the via size and line width/spacing are limiting process constraints that hinder the use of LTCC at submillimeter-wave frequencies. Another technology to fabricate waveguide slot antenna arrays up to 350 GHz is metal diffusion bonding, which utilizes interdiffusion of atoms across the interface to bond the antenna feeding network layer and the radiating slot layer [12]. It is worth noting that all the aforementioned antenna fabrication techniques have disadvantages of high tooling and equipment cost, long lead time for small-volume prototyping or production. Until recently, the proliferation of additive manufacturing (AM) or 3D Printing (3DP) has opened new opportunities for low-cost, rapid, and on-demand manufacturing of mmW and THz antennas and components [13]-[16]. A dielectric material jetting technique in [14] is used to 3D print a horn antenna working at 105 GHz based on hollow-core electromagnetic crystal (EMXT) waveguide. The resulting horn structure is shown a lack of dielectric to waveguide transition; thus, it is very challenging to measure the antenna and couple it with other components. Metal printed horn antennas have also been investigated up to 352 GHz [16]. Measurement results show the gain degradation is mainly caused by the increased surface roughness of the printed metal as compared to the smooth copper.

While research interest continues to expand in 3D printing of mmW and sub-mmW antennas, most of the previous works focus on the design of horn and lens antennas with large electrical size. Though the large aperture reflectarray [13] shows good performance, it needs dedicated feed and supporting fixtures to accurately control the focal length, which leads to a heavy and bulky antenna system. There are still very few compact, lightweight all-metal antennas that can be 3D printed to operate above 100 GHz. This paper presents a D-band, compact antenna based on the resonant cavity antenna (RCA) concept [17]-[19]. RCAs have been investigated mostly in microwave bands employing planar antenna feeds and dielectric-based superstrate [20] - [23]. At frequencies above 100 GHz, these designs depend on the accurate control of the cavity height, which is difficult to be manually assembled. Also, the unit cell size of PRS becomes small, and the cost of patterning the PRS onto high-end low-loss dielectric materials is increased. An all-metal RCA with built-in cavity can alleviate above-mentioned problems. The present antenna can be produced in a single production cycle. The self-supporting antenna structure integrates directly to a standard WR-6 waveguide port, and the directivity of the waveguide feed can be enhanced to form a directive beam. Both dielectric and metal additive manufacturing methods are used to print the prototypes. The resultant antenna shows a measured radiation efficiency of 70%, 20 GHz of 3-dB gain bandwidth, and 15.5 dBi maximum gain at 135 GHz. The antenna as printed performs well without the need for expensive and time-consuming postprocessing. To the best of authors' knowledge, the proposed work is the first demonstration of D-band resonant cavity antennas fabricated by commercially available printers. This paper is organized as follows. The antenna design principle is described in Section II. Details of manufacturing processes are presented in Section III. In Section IV, we demonstrate and discuss the performance of the printed antennas by comparing the simulated and measured results. Finally, conclusions are made in Section V.

II. ANTENNA DESIGN CONCEPT

A. *RCA Principle of Operation*

The antenna structure consists of a partially reflective surface (PRS) as the superstrate and a feed antenna with a ground plane, as shown in Fig. 1. The PRS superstrate can reflect part of the incidence wave, the rest of which leaks into the free space. Therefore, the incident wave launched into the parallel plate cavity formed by the PRS and ground plane undergoes multiple reflections inside the cavity. There is strong resonance inside the antenna cavity. Through proper control of the constructive interference of reflected/transmitted waves, the low directivity of the feed antenna can be enhanced, forming a high directivity beam. Here we use ray tracing to analyze the leaky wave behaviors of RCA [24]. Consider, first of all, the reflection coefficient of the PRS to be $Re^{j\varphi_{PRS}}$. Phase shifts of the rays transmitted through the PRS are introduced by the path length, the ground plane and the phase of the PRS reflection coefficient φ_{PRS}. The electric field at the antenna far-field is superposition of the leaked waves and can be expressed as

$$E=\sum_{n=0}^{\infty} f(a)\,E_0R^n\sqrt{1-R^2}e^{j\varphi_n} \tag{1}$$

where $f(a)$ is the radiation pattern of the source, E_0 is the maximum E-field strength, and φ_n is the phase difference between the emergent rays. If we define $\emptyset$ as the phase difference of the neighboring rays, φ_n can be calculated:

$$\varphi_n = n\times\emptyset = n\left(\varphi_{PRS}-\pi-\frac{4\pi h_c}{\lambda}cos\theta\right) \tag{2}$$

where h_c is the cavity depth, λ is the free-space wavelength. Since $R<1$, the directivity of the RCA can be obtained by:

$$D=\frac{1-R^2}{1-R^2-2Rcos(\varphi_n)} \tag{3}$$

To form a focused beam at the broadside $(\theta=0)$ with a maximum directivity, $cos(\varphi_n)$ in the above equation needs to be zero, thus from (2) and (3) we can derive:

$$h_c=\left(\frac{\varphi_{PRS}}{2\pi}-\frac{1}{2}\right)\frac{\lambda}{2}+N\frac{\lambda}{2}, where\ N=0,1,2,\ldots \tag{4}$$

$$D(dB)=10\log\left(\frac{1+R}{1-\mathrm{R}}\right) \tag{5}$$

From (5), a PRS with a higher magnitude of reflection coefficient R can yield a higher directivity. However, the half-power gain bandwidth decreases as R increases. The solution to PRS superstrate used in our design is a metallic grid, chosen since this type of structure is more suitable to be additively manufactured than the one etched on thin substrates. Most RCA designs at microwave frequencies use a frequency selective surface (FSS) based superstrate, and the cavity depth is controlled by screws positioned at the four corners in between the superstrate and ground plane [22]. At mmW/THz frequencies, this approach faces problems such as the higher

This article has been accepted for publication in a future issue of this journal, but has not been fully edited. Content may change prior to final publication. Citation information: DOI 10.1109/TTHZ.2020.2986650, IEEE Transactions on Terahertz Science and Technology

dielectric loss and inaccuracy of the cavity depth (accuracy in the order of 0.1 mm at 300 GHz) when a manual assembly of the antenna is sought.

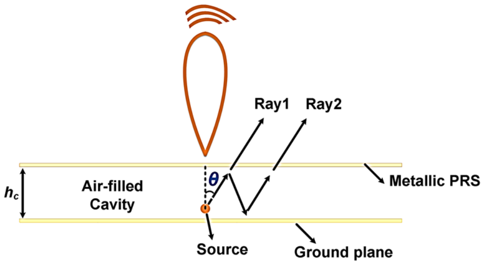

Fig. 1. Illustration (side view) of the RCA working mechanism.

Fig. 2 shows the D band all-metal RCA configuration comprising a PRS, an impedance matching layer (IML), and a standard waveguide feed (WR-6). First, the unit cell of the PRS is optimized following two general rules: i) larger reflection magnitude results in higher antenna gain, but the resulting impedance matching would not be practically tunable due to the strong resonances inside the cavity. Also, the Q factor is so high that the gain-bandwidth product is narrow; ii) the antenna reflection coefficient is dependent on the dimensions of the unit cell. In practice, it is of importance to finetune the parameters of the unit cell in order to use the commercially available 3D printers to fabricate the resulting antenna. As a compromise, a relatively low reflection coefficient is adopted to achieve a moderate gain. Parametric studies of the two key parameters (a, t in Fig. 2) to fine-tune the magnitude and phase of the reflectivity response are shown in Fig. 3, and Fig. 4. Since the realized antenna gain is proportional to the reflection magnitude, as given in (5), the smaller unit cell aperture lateral size a has less reflection magnitude change over frequency, thus producing flatter antenna directivity versus frequency curve. It can be seen that the reflection magnitude is less sensitive to the change of unit cell layer thickness t, which is a limiting parameter for the practical antenna fabrication. At the operating frequency f_o, the reflection phase φ_{PRS} of the PRS is obtained through unit cell simulation to determine an initial cavity thickness h_c by using (4).

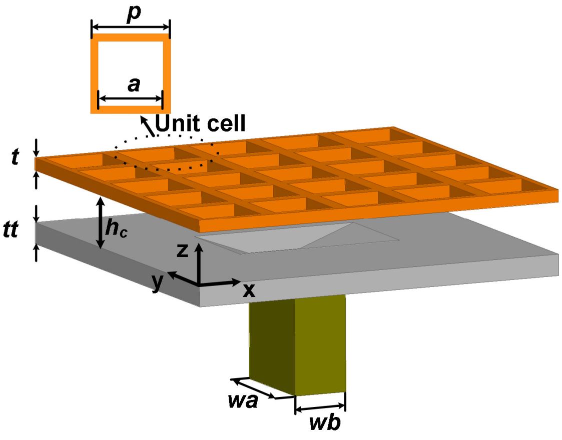

(a)

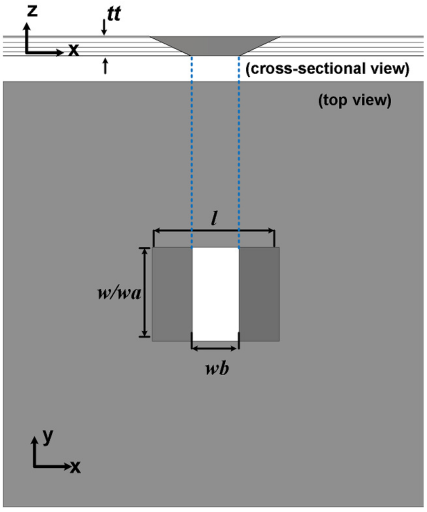

(b)

Fig. 2. Antenna schematic view (a) and IML configuration (b).

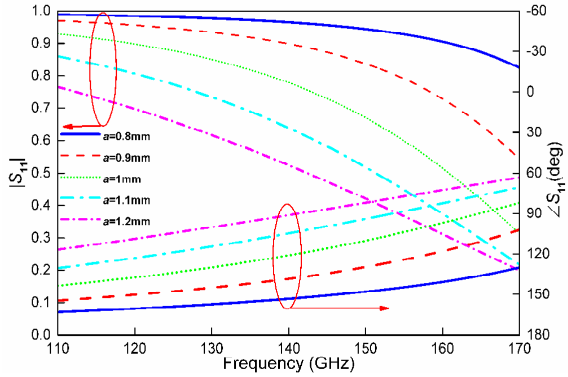

Fig. 3. Parametric study of unit cell periodicity a.

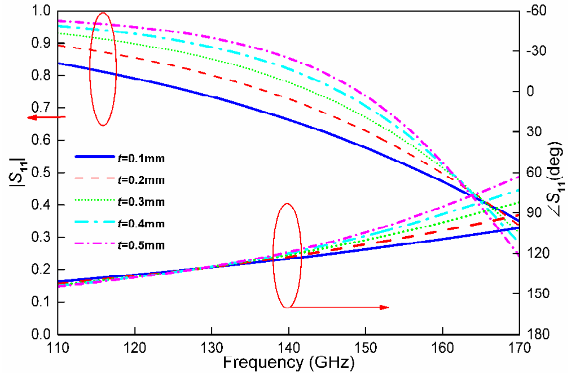

Fig. 4. Parametric study of PRS layer thickness t.

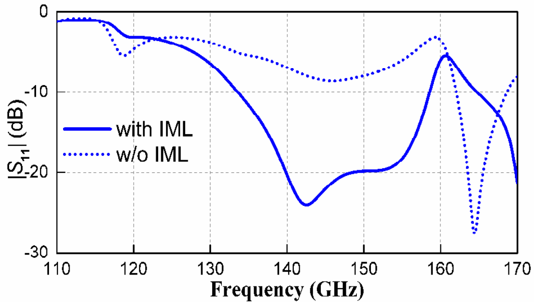

Fig. 5. Simulated antenna impedance matchings w/ and w/o proposed transition.

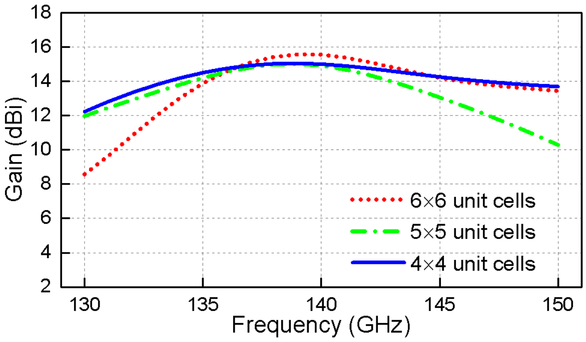

Fig. 6. Gain comparison of different aperture sizes.

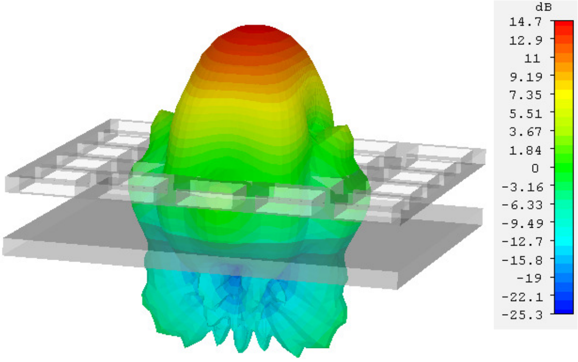

Fig. 7. Simulated antenna radiation pattern at 140 GHz.

Fig. 5 shows the computed reflection coefficients of the antenna shown in Fig. 2. It is evident that the RCA can operate with a below -10 dB reflection coefficient from 134 GHz to 158 GHz by introducing the impedance matching layer consisting of a shallow horn transition between the waveguide feed aperture and antenna cavity. By introducing the quasi-horn impedance matching layer, the impedance of the feed can be gradually transformed to achieve an excellent impedance matching over a 20 GHz bandwidth. Fig. 6 shows the gain comparison of three PRS configurations. The maximum gain of the RCA is shown to have less than 1 dB enhancement by increasing the aperture size. It is depicted in Fig. 7 that, for the 5 × 5 unit cell PRS, the simulated radiation pattern is directive in the broadside with a gain of 14.7 dBi.

B. Gain Enhancement

To improve the performance of the antenna in Fig. 2, some critical modifications are required, and the final antenna dimensions need to be printable using suitable 3DP techniques. The resultant antenna configuration is shown in Fig. 8.

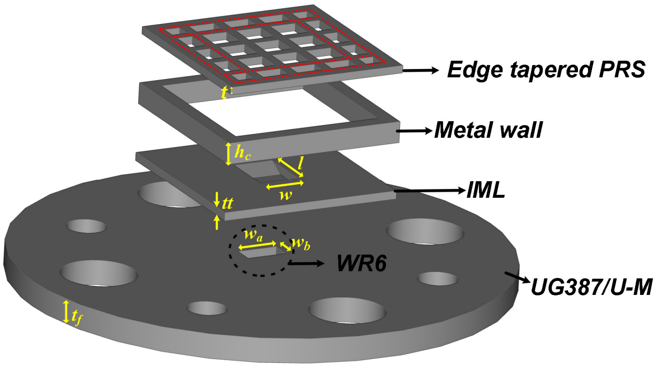

(a)

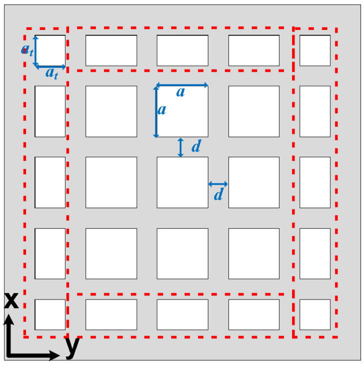

(b)

Fig. 8. (a) Exploded view of the antenna configuration; (b) top view of the PRS. Final parameter values of the optimized antenna a = 1.07 mm, a_t = 0.64 mm, d = 0.43 mm, t = 0.3 mm, tt = 0.33 mm, t_f = 1 mm, h_c = 0.86 mm, w = 1.65 mm, l = 2.24 mm, w_a = 1.65 mm, w_b = 0.83 mm.

For ease of measurement, we integrate the standard waveguide flange into the antenna design. Built on the UG387 flange base, the RCA consists of a tapered PRS supported by a metal wall spacer. The feed waveguide is a standard WR 6 with aperture of $w_a \times w_b$ (2.54 mm × 1.27 mm). As shown in Fig. 8 (b), the center 3 × 3 PRS unit cells have the same periodicity and lateral size while the other unit cells along the edges have smaller sizes. The entire PRS structure is symmetric with respect to the x and y-axis. The WR6 waveguide feed is directly connected to the IML. It is worth noting that adding the supporting metal wall and tapering the sizes of unit cells at the four edges are two important methods to improve not only the mechanical stability but also the overall antenna performance. First, enclosure by the four metal walls leads to antenna structure stability, and the cavity thickness can be accurately defined by the height of the metal wall. Second, the antenna impedance matching along with the radiation efficiency can be improved by tapering the lateral length of the square unit cell aperture. Fig. 9 shows that the antenna impedance matching can be further improved by introducing the unit cell tapering and metal wall. Moreover, the antenna gain is increased by approximately 1.5 dB by using both PRS tapering and wall enclosure methods, as shown in Fig. 10. It is clear in Fig. 11 that the side lobes and back lobes of the RCA are significantly reduced by introducing the supporting walls and tapering of the PRS. Fig. 12 indicates the tapered PRS antenna has a larger effective aperture excited than the non-tapered PRS antenna. The reason is because the unit cell is almost halved, and the co-polarized wave is mostly blocked at the aperture edge.

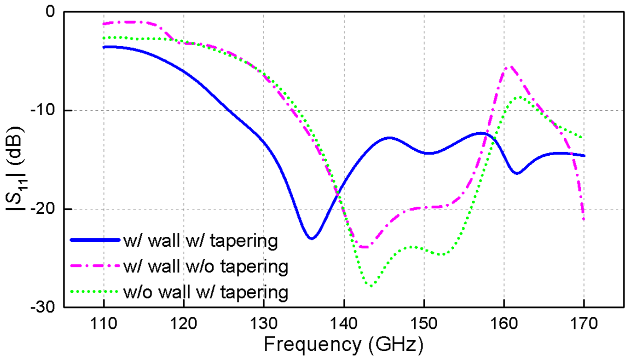

Fig. 9. Simulated reflection coefficients in the D band.

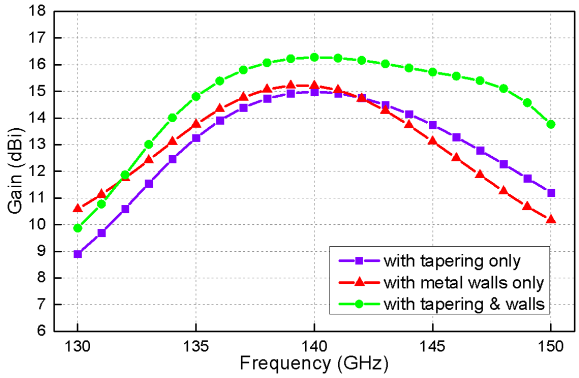

Fig. 10. Simulated D-band antenna gains with different configurations.

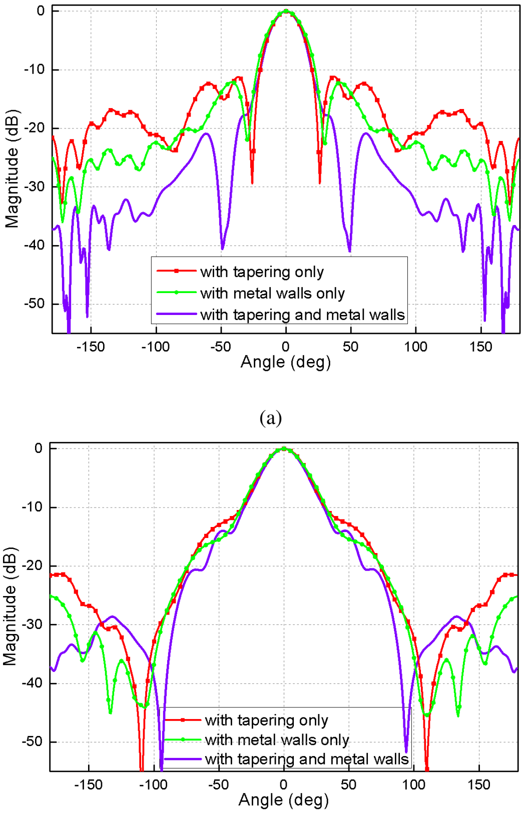

(a)

(b)

Fig. 11. Simulated D-band antenna radiation patterns: (a) E-plane; (b) H-plane.

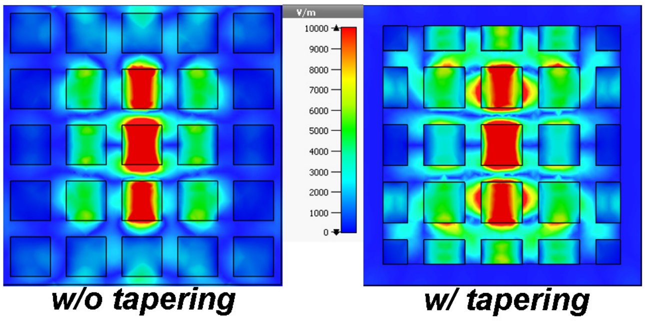

Fig. 12. Simulated E-field distribution across the PRS aperture with and without edge tapering of the PRS.

III. Antenna Additive Manufacturing

A number of different 3DP techniques have been developed in recent years, most of which can be divided into two main categories: polymer/dielectric 3DP and all-metal 3DP. As the operating band steps into the mmW ranges, the quality of the printed parts is of great importance to the resulting antenna performance. Printing resolution, structural limitations, and surface finish are among many intangible factors that are key to a functional antenna part. Due to the small wavelength, mmW/THz antennas tend to have fine geometry details, which impose stringent requirements on the manufacturing methods. It is generally desirable to use the commercial 3D printers that can achieve high spatial resolution, small build layer thickness, and low surface roughness. Table I summarizes the viable 3DP techniques reported for producing millimeter-wave components. Next, we describe two 3DP techniques used to produce the proposed RCA.

Table I Comparison of different 3DP techniques

3DP processes	Min. wall thicknesses	Min. layer thickness	Min. surface roughness RMS	Tolerance
Dielectric printing				
Vat Polymerization (SLA, DLP)	0.1 mm	16μm	1 μm	±0.15mm
Material Jetting	0.3 mm	16μm	2μm	±0.025mm
Metal Printing				
Powder Bed Fusion (SLM, DMLS, EBM)	0.2 mm	20μm	12 μm as printed	±0.0254mm
Binder Jetting	0.15 mm	42μm	3 μm	±0.13mm

A. *Metal Coated Polymer Antenna*

Material Jetting (MJ) has demonstrated its capability of additively manufacturing THz components [25]. The polymeric antenna components were printed using a Stratasys J750 industrial-grade 3D printer. The printer produces models by jetting thin layers of printing materials on the build tray until the complete model is formed. UV light sources attached to the print heads are used to immediately cure the sprayed resin. After an entire layer is finished, the build platform drops one layer in height, and the process is repeated until the entire part is complete. To print objects with different hardness, flexible, and rigid model materials are digitally printed in different ratios. The antenna part shown in Fig. 13 was finally built with a layer thickness of 14 µm in 20 minutes.

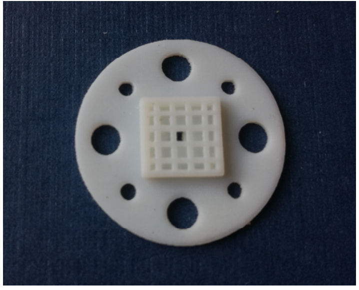

Fig. 13. As printed polymer antenna part using VeroPureWhite (RGD837).

Electroplating is a common method to metal plate the dielectric part. To make a conductive seed layer, the antennas were coated with a thin layer of platinum using a physical vapor deposition (PVD). PVD is a vacuum metallization process where a metal vapor is created by the bombardment of a solid target with gaseous Argon ions. This vapor is then deposited on the antenna forming a thin metallic film. Due to the directivity of the process, the antenna is not only placed on a rotating table in the vacuum chamber, but the process is also repeated up to 5 times while reorienting the antenna around each time to improve the coverage of the part. Fig. 14 shows the copper-plated antenna surface. The polymer antenna samples fabricated from the VeroPureWhite, RGD837 material, had improper coverage due to the outgassing of the polymer. This was most pronounced at the sidewalls of the 3D-printed part. After PVD coating, the seed layer was thickened to about 10 µm by copper plating. Although the described process produced acceptable results for a proof of concept, much improvement can be made to improve the durability, coverage, and quality of the metallization.

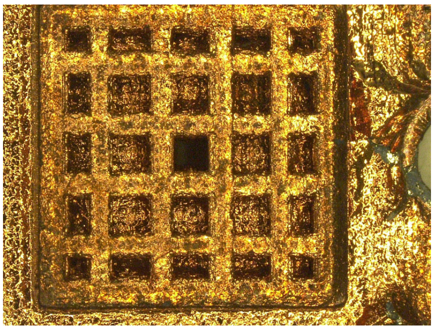

Fig. 14. Microscopic view of the PVD coated antenna surface.

B. *Metal Printed Antenna*

The most attractive feature of metal 3DP is the feasibility of producing the final parts that can be used for end-use applications without any post-processing, thus saving time and labor. Direct metal laser sintering (DMLS) is an industrial 3DP process that has been implemented to prototype mmW waveguides [26]. Typical material options are Aluminum AlSi10Mg and Stainless Steel 316L. Parts printed by using Stainless Steel 316L have excellent corrosion resistance and can be further polished like conventionally produced stainless steel parts while the lightweight AlSi10Mg material has slightly worse part accuracy. The DMLS process begins with melting the first layer onto a metal build plate. Each layer is melted with a high-power fiber laser, melting the powder (5-63 µm) in the appropriate areas as controlled by the computer-aided design (CAD) model. The process is repeated layer by layer until the desired part is created, which takes 1.5 - 2 hours. The cost for manufacture via DMLS is material sensitive, indicative costs for the two antennas are below $200 using 316L and AlSi10Mg. Fig. 15 shows that the printed 316L antenna can be directly mounted to the standard waveguide flange (UG387/UM) of the test port.

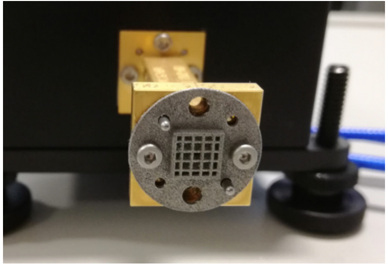

Fig. 15. Printed all-metal antenna (stainless 316L) without polishing.

The surface roughness of the fabricated metallic antennas (and polymeric for comparison) was measured (Table II), using white light interferometry (Dektak XTL, Bruker, UK). The measured results are shown in Fig. 16. Print resolution for DMLS is limited by a combination of powder particle size and laser beam spot diameter. The potential for higher resolution and improved surface quality may be realized through the use of specialized Powder Bed Fusion (PBF) technology that uses a thermal source that induces fusion (sintering or melting) between the particles of a plastic or metal powder one layer at a time.

TABLE II SURFACE ROUGHNESS VALUES FOR 3DP ANTENNAS

Antenna Material	Ra (µm)
AlSi10Mg	12±2
316L	16±2
VeroPureWhite, RGD837	2.0±0.4

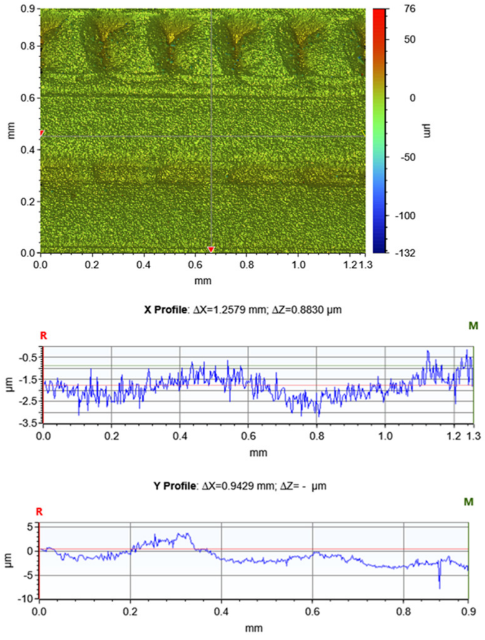

(a)

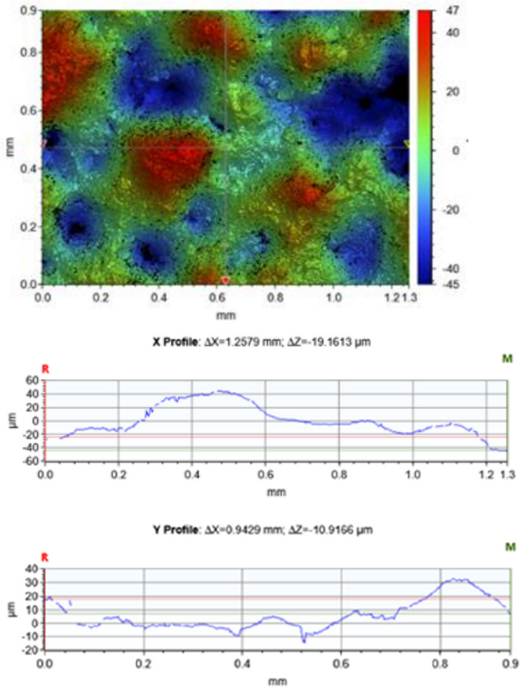

(b)

Fig. 16. Measured surface roughness for (a) polymer antenna sample; (b) metallic antenna sample.

IV. ANTENNA EXPERIMENTAL RESULTS

The proposed RCA is fabricated with overall sizes of 7 mm × 7 mm × 2.5 mm. Measurements were performed in the lab of ESAT, KU Leuven. Fig. 17 shows the measurement setup. RF signals are generated with an Agilent PSG and then multiplied by 12 to the D-band frequency range with an R&S VNA extender. The antenna under test is mounted on the waveguide flange of the frequency extender, and the whole setup is placed on top of a rotational stage from Thorlabs. The receiving antenna is a standard D-band horn antenna (around 24 dBi gain), and the received signal is down-converted with a subharmonic mixer prior to measuring its power with an R&S spectrum analyzer. The measurement setup is controlled by a computer using MATLAB. For the antenna gain measurements, first, a "through" measurement is performed with two Millitech D-band horn antennas with known gain (from the datasheet). Next, one of them is replaced with the antenna under test, and a comparative measurement is done to determine the gain of antenna under test.

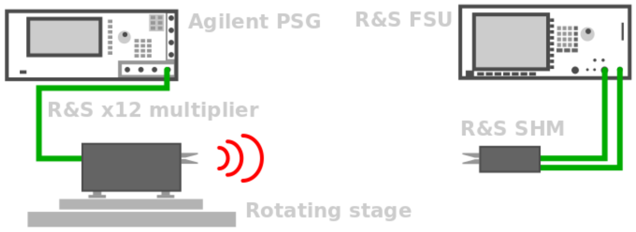

(a)

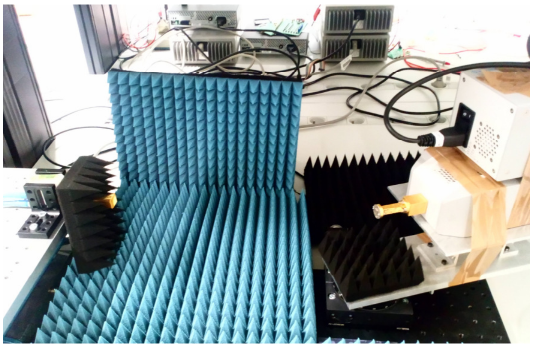

(b)

Fig. 17. Antenna measurement setup: (a) schematics; (b) pattern measurement.

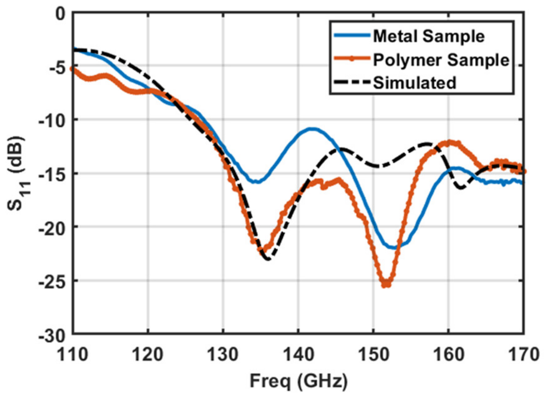

Fig. 18. Measured reflection coefficients of the two printed antenna prototypes.

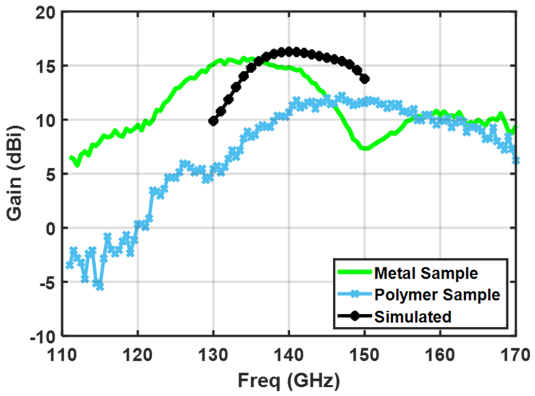

Fig. 19. Measured peak gains of the two printed antenna prototypes.

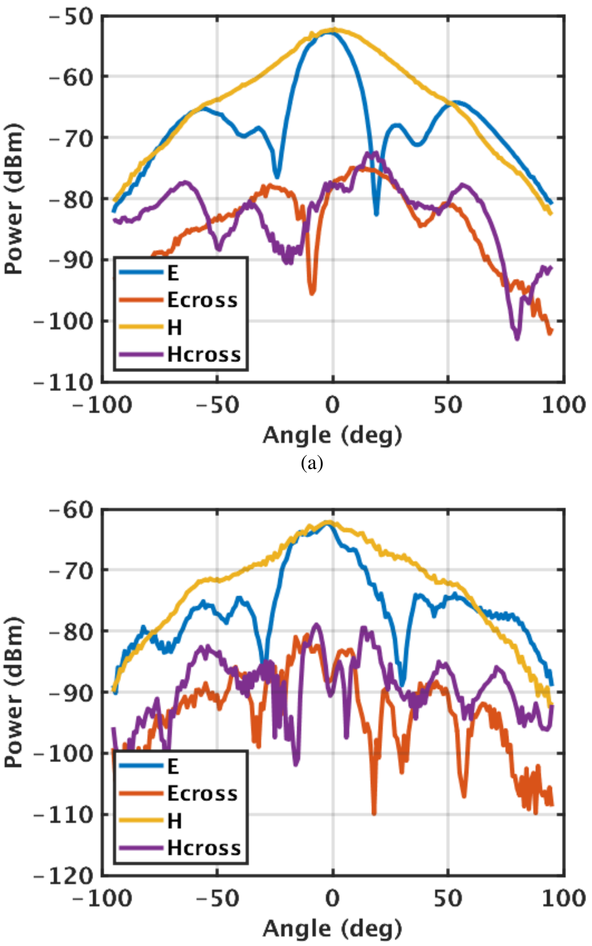

(a)

(b)

Fig. 20. Measured radiation patterns at 135 GHz; (a) metal printed antenna; (b) polymer printed antenna.

The measured reflection coefficients of the two antenna samples show good agreement with the simulated results, as depicted in Fig. 18. A broad -10 dB S_{11} frequency range is observed, covering from 126 GHz to 170 GHz.

Fig. 19 shows the simulated and measured gain. It is noted that for the metal printed antenna, the gain peaks at the frequency of 135 GHz with a value of 15.5 dBi, which is a 5-GHz, 3% shift from the design center frequency (f_0 = 140 GHz). It appears that the antenna frequencies of operation are downshifted. The achieved gain peak is 1 dB less than the simulated one, which is mainly due to the metal losses. As for the copper-coated polymer sample, the maximum gain is about 12.1 dBi at 146 GHz. The gain curve shifts upwards. There is about 4 dB gain reduction, which is speculated to result from the metallization processes. It is highly likely that the inner surfaces of the PRS and metal cavity are not fully metal plated. For both the antenna samples, the gain shift in frequency may be caused by the inaccuracy of the cavity thickness h_c during the 3DP processes. The measured radiation patterns at the gain peak for the two antenna prototypes are shown in Fig. 20. The metal printed sample exhibits a narrower beamwidth in E-plane with a half-power beamwidth (HPBW) of 30°. The maximum cross-polarization level is below -20 dB within the antenna HPBW angle range. As regards to the polymer sample, the plot shows asymmetry beam pattern in E-plane. We assess the reason is that the polymer material is soft after printing, which leads to some bending of the thin PRS superstrate. It is noted that the two antennas have a sidelobe level of better than -13 dB at E/H planes.

Table III compares the reported mmW antennas fabricated by different 3DP techniques. It is clear that the proposed RCA has the smallest effective aperture size with a moderate gain. Also, the low profile (total height of 2.5 mm) of the presented antenna permits a compact system when the antenna is connected to a chip through a chip to waveguide transition.

TABLE III COMPARISON OF 3D PRINTED MMW ANTENNAS

Ref No	Fabrication process	Max. size	Operating frequency	Gain	Aperture efficiency
[13]	MJ	10λ	100 GHz	25 dBi	74.2%
[14]	MJ	12λ	140 GHz	20 dBi	84.8%
[15]	SLA	15λ	250 GHz	24 dBi	68.9%
[16]	DMLS	23λ	140 GHz	23.75 dBi	79.6%
This work	DMLS	3λ	140 GHz	15.5 dBi	77.5%(max.)
	MJ			12.1 dBi	

A sample of the metal 3D-printed antenna was coupled into a system together with the transmitter presented in [27]. Fig. 21 illustrates the CMOS transmitter's schematic. The continuous phase frequency-shift keying (CPFSK) transmitter is implemented by a 140 GHz digitally controlled oscillator followed up by a power amplifier. This frequency source can deliver up to 7dBm output power, which is then fed to the antenna through a ground-signal-ground (GSG) to waveguide transition delivering a measured output power of 5 dBm at 142 GHz to the antenna [28]. The performance of the system was verified by measuring the effective isotropic radiated power (EIRP) with a subharmonic mixer and spectrum analyzer. An EIRP of 19 dBm was achieved around the expected level. The ultra-low profile of the antenna makes it a low-cost, attractive alternative to the CNC machined horn antennas when employed in miniaturized transceiver modules [29].

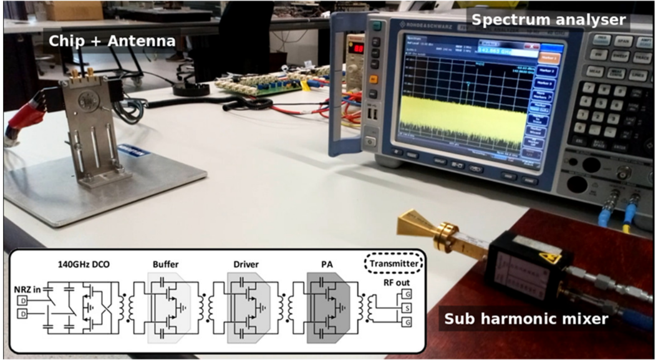

Fig. 21. Measurement setup for characterizing the transmitter integrating the metal printed antenna with the CMOS chip.

V. CONCLUSION

A low-profile all-metal antenna design with resonant cavity configurations is shown to form directive beams in the frequency range of 130-150 GHz. The antenna has an advantage of direct integration of the waveguide feed and partially reflecting surface into a single antenna configuration. The optimization of the antenna performance is achieved by tuning the impedance matching transition and lateral sizes of the PRS unit cells. Thanks to the commercially available 3D printing techniques, the proposed antenna concept is successfully prototyped and verified by experimental results. It is shown that the resulting antenna has a wide bandwidth and a maximum gain of 15.5 dBi with directive beam patterns at 135 GHz. The presented antenna can be readily assembled into any transceivers that have a standard waveguide interface. Moreover, because of the all-metal structure, the antenna can be scaled to other frequency bands. Successful demonstration of the proposed antenna proves the great potential to employ additive manufacturing to produce antennas operating beyond 100 GHz directly from CAD files for rapid prototyping and production, with reduced costs.

VI. ACKNOWLEDGEMENTS

This work is funded by CHIST ERA WISDOM project under EPSRC grant EP/P015840/1, EPSRC grants EP/S005625/1, EP/N032497/1, and the EPSRC HVM Catapult Fellowship scheme grant REF: EP/ L017121/1.

REFERENCES

[1] C. Jansen, S. Wietzke, M. Scheller, N. Krumbholz, C. Järdens, K. Baaske, T. Hochrein, M. Koch, and R. Wilk, "Applications for THz systems: Approaching Markets and perspectives for an Innovative Technology," *Opt. Photon.*, vol. 3, no. 4, pp. 26–30, 2008, doi: 10.1002/opph.201190218.

[2] M. Fujishima, "Key Technologies for THz Wireless Link by Silicon CMOS Integrated Circuits," *Photonics*, vol. 5, no. 4, p. 50, Nov. 2018, doi: 10.3390/photonics5040050.

[3] H.-J. Song, 'Packages for Terahertz Electronics', Proc. IEEE, vol. 105, no. 6, pp. 1121–1138, Jun. 2017, doi: 10.1109/JPROC.2016.2633547.

[4] D. Rutledge, "Substrate-lens coupled antennas for millimeter and submillimeter waves," *IEEE Antennas Propag. Soc. Newsl.*, vol. 27, no. 4, pp. 4–8, 1985, doi: 10.1109/MAP.1985.27816.

[5] J. Al-Eryani, H. Knapp, J. Kammerer, K. Aufinger, H. Li, and L. Maurer, "Fully Integrated Single-Chip 305–375-GHz Transceiver With On-Chip Antennas in SiGe BiCMOS," *IEEE Trans. THz Sci. Technol.*, vol. 8, no. 3, pp. 329–339, May 2018, doi: 10.1109/TTHZ.2018.2823202.

[6] H.-J. Song, J.-Y. Kim, K. Ajito, M. Yaita, and N. Kukutsu, 'Fully Integrated ASK Receiver MMIC for Terahertz Communications at 300 GHz', IEEE Trans. THz Sci. Technol., vol. 3, no. 4, pp. 445–452, Jul. 2013, doi: 10.1109/TTHZ.2013.2252954.

[7] H.-J. Song, H. Matsuzaki, and M. Yaita, 'Sub-Millimeter and Terahertz-Wave Packaging for Large Chip-Width MMICs', IEEE Microw. Wireless Compon. Lett., vol. 26, no. 6, pp. 422–424, Jun. 2016, doi: 10.1109/LMWC.2016.2537789.

[8] B. Pan, Y. Li, G. E. Ponchak, J. Papapolymerou, and M. M. Tentzeris, 'A 60-GHz CPW-Fed High-Gain and Broadband Integrated Horn Antenna', IEEE Trans. Antennas Propagat., vol. 57, no. 4, pp. 1050–1056, Apr. 2009, doi: 10.1109/TAP.2009.2015815.

[9] C. Lee et al., 'Terahertz antenna arrays with silicon micromachined-based microlens antenna and corrugated horns', in 2015 International Workshop on Antenna Technology (iWAT), Seoul, 2015, pp. 70–73, doi: 10.1109/IWAT.2015.7365264.

[10] M. Alonso-delPino, T. Reck, C. Jung-Kubiak, C. Lee, and G. Chattopadhyay, 'Development of Silicon Micromachined Microlens Antennas at 1.9 THz', IEEE Trans. THz Sci. Technol., vol. 7, no. 2, pp. 191–198, Mar. 2017, doi: 10.1109/TTHZ.2017.2655340.

[11] J. Xu, Z. N. Chen, X. Qing, and W. Hong, "140-GHz Planar Broadband LTCC SIW Slot Antenna Array," *IEEE Trans. Antennas Propag.*, vol. 60, no. 6, pp. 3025–3028, Jun. 2012, doi: 10.1109/TAP.2012.2194673.

[12] K. Tekkouk, J. Hirokawa, K. Oogimoto, T. Nagatsuma, H. Seto, Y. Inoue, and M. Saito, "Corporate-Feed Slotted Waveguide Array Antenna in the 350-GHz Band by Silicon Process," *IEEE Trans. Antennas Propag.*, vol. 65, no. 1, pp. 217–225, Jan. 2017, doi: 10.1109/TAP.2016.2631132.

[13] P. Nayeri, M. Liang, R. A. Sabory-Garcı´a, M. Tuo, F. Yang, M. Gehm, H. Xin, and A. Z. Elsherbeni, "3D Printed Dielectric Reflectarrays: Low-Cost High-Gain Antennas at Sub-Millimeter Waves," *IEEE Trans. Antennas Propag.*, vol. 62, no. 4, pp. 2000–2008, Apr. 2014, doi: 10.1109/TAP.2014.2303195.

[14] Z. Wu, M. Liang, W.-R. Ng, M. Gehm, and H. Xin, "Terahertz Horn Antenna Based on Hollow-Core Electromagnetic Crystal (EMXT) Structure," *IEEE Trans. Antennas Propag.*, vol. 60, no. 12, pp. 5557–5563, Dec. 2012, doi: 10.1109/TAP.2012.2211318.

[15] H. Yi, S.-W. Qu, K.-B. Ng, C. H. Chan, and X. Bai, "3-D Printed Millimeter-Wave and Terahertz Lenses with Fixed and Frequency Scanned Beam," *IEEE Trans. Antennas Propag.*, vol. 64, no. 2, pp. 442–449, Feb. 2016, doi: 10.1109/TAP.2015.2505703.

[16] B. Zhang, Z. Zhan, Y. Cao, H. Gulan, P. Linner, J. Sun, T. Zwick, and H. Zirath, "Metallic 3-D Printed Antennas for Millimeter- and Submillimeter Wave Applications," *IEEE Trans. THz Sci. Technol.*, vol. 6, no. 4, pp. 592–600, Jul. 2016, doi: 10.1109/TTHZ.2016.2562508.

[17] C. Gu, S. Gao, and B. Sanz-Izquierdo, 'Low-cost wideband low-THz antennas for wireless communications and sensing', in 2017 10th UK-Europe-China Workshop on Millimetre Waves and Terahertz Technologies (UCMMT), Liverpool, United Kingdom, 2017, pp. 1–4, doi: 10.1109/UCMMT.2017.8068470.

[18] C. Gu, S. Gao, and B. Sanz-Izquierdo, 'Wideband low-THz antennas for high-speed wireless communications', in 2017 IEEE-APS Topical Conference on Antennas and Propagation in Wireless Communications (APWC), Verona, Italy, 2017, pp. 141–145, doi: 10.1109/APWC.2017.8062263.

[19] C. Gu et al., 'Wideband high-gain millimetre/submillimetre wave antenna using additive manufacturing', IET Microwaves, Antennas & Propagation, vol. 12, no. 11, pp. 1758–1764, Sep. 2018, doi: 10.1049/iet-map.2018.5412.

[20] A. Foroozesh and L. Shafai, "On the Characteristics of the Highly Directive Resonant Cavity Antenna Having Metal Strip Grating Superstrate," *IEEE Trans. Antennas Propag.*, vol. 60, no. 1, pp. 78–91, Jan. 2012, doi: 10.1109/TAP.2011.2167933.

[21] Y. Sun, Z. N. Chen, Y. Zhang, H. Chen, and T. S. P. See, 'Subwavelength Substrate-Integrated Fabry-Pérot Cavity Antennas Using Artificial Magnetic Conductor', IEEE Trans. Antennas Propagat., vol. 60, no. 1, pp. 30–35, Jan. 2012, doi: 10.1109/TAP.2011.2167902.

[22] X.-X. Yang, G.-N. Tan, B. Han, and H.-G. Xue, 'Millimeter Wave Fabry-Perot Resonator Antenna Fed by CPW with High Gain and Broadband', International Journal of Antennas and Propagation, vol. 2016, pp. 1–7, 2016, doi: 10.1155/2016/3032684.

[23] F. Meng and S. K. Sharma, "A Wideband Resonant Cavity Antenna with Compact Partially Reflective Surface," *IEEE Trans. Antennas Propag.*, pp. 1–1, 2019, doi: 10.1109/TAP.2019.2938589.

[24] G. V. Trentini, "Partially reflecting sheet arrays," *IRE Trans. Antennas Propag.*, vol. AP-4, pp. 666–671, Oct. 1956, doi: 10.1109/TAP.1956.1144455.

[25] H. Xin and M. Liang, "3-D-Printed Microwave and THz Devices Using Polymer Jetting Techniques," *Proc. IEEE*, vol. 105, no. 4, pp. 737–755, Apr. 2017, doi: 10.1109/JPROC.2016.2621118.

[26] M. Holmberg, D. Dancila, A. Rydberg, B. Hjörvarsson, U. Jansson, J. J. Marattukalam, N. Johansson, and J. Andersson, "On Surface Losses in Direct Metal Laser Sintering Printed Millimeter and Submillimeter Waveguides," *J Infrared Milli Terahz Waves*, vol. 39, no. 6, pp. 535–545, Jun. 2018, doi: 10.1007/s10762-018-0470-x.

[27] M. De Wit, Y. Zhang, and P. Reynaert, "Analysis and design of a foam-cladded PMF link with phase tuning in 28-nm CMOS," *IEEE J. Solid-State Circuits*, vol. 54, no. 7, pp.1960–1969, Apr. 2019, doi: 10.1109/JSSC.2019.2907163.

[28] Y. Zhang, D. Zhao, and P. Reynaert, "A flip-chip packaging design with waveguide output on single-layer alumina board for E-band applications," *IEEE Trans. Microw. Theory Techn.*, vol. 64, no. 4, pp. 1255–1264, Apr. 2016, doi: 10.1109/TMTT.2016.2536602.

[29] T. Jaeschke, C. Bredendiek, S. Kuppers, and N. Pohl, "High-Precision D-Band FMCW-Radar Sensor Based on a Wideband SiGe-Transceiver MMIC," *IEEE Trans. Microwave Theory Techn.*, vol. 62, no. 12, pp. 3582–3597, Dec. 2014, doi: 10.1109/TMTT.2014.2365460.

This article has been accepted for publication in a future issue of this journal, but has not been fully edited. Content may change prior to final publication. Citation information: DOI 10.1109/TTHZ.2020.2986650, IEEE Transactions on Terahertz Science and Technology

Chao Gu received the B.S. and M.S. degrees from Xidian University, Xi'an, China, in 2009 and 2012, respectively, and the Ph.D. degree from the University of Kent, Canterbury, U.K., in 2017. He is currently with the Centre for Wireless Innovation, ECIT Institute, School of Electronics, Electrical Engineering and Computer Science, Queen's University Belfast, Belfast, U.K. His research interests include phased array antennas, reconfigurable antennas, and frequency selective surfaces.

Steven Shichang Gao (M'01-SM'16-F'19) received the PhD from Shanghai University, China. He is a Full Professor and Chair in RF and Microwave Engineering, and the Director of Graduate Studies at the School of Engineering and Digital Arts, University of Kent, UK. His research covers smart antennas, phased arrays, MIMO, reconfigurable antennas, broadband/multiband antennas, satellite antennas, RF/microwave/mm-wave/THz circuits, mobile communications, satellite communications, UWB radars, synthetic-aperture radars, IoT and sensors for healthcare. He co-authored/co-edited three books (Space Antenna Handbook, Wiley, 2012; Circularly Polarized Antennas, IEEE-Wiley, 2014; Low-Cost Smart Antennas, Wiley, 2019), over 300 papers and 10 patents. He was a Distinguished Lecturer of IEEE Antennas and Propagation Society and serves as an Associate Editor for several international Journals (IEEE Transactions on Antennas and Propagation; Radio Science; IEEE Access; Electronics Letters; IET Circuits, Devices and Systems, etc), and the Editor-in-Chief for John Wiley & Sons Book Series on "Microwave and Wireless Technologies". He was General Chair of LAPC 2013, and an Invited Speaker at many conferences. He is a Fellow of IEEE, and also a Fellow of Royal Aeronautical Society, UK, and the IET, UK.

Vincent Fusco (S'82–M'82–SM'96–F'04) received the bachelor's degree (Hons.) in electrical and electronic engineering, the Ph.D. degree in microwave electronics, and the D.Sc. degree from Queen's University Belfast (QUB), Belfast, U.K., in 1979, 1982, and 2000, respectively. He is currently the Chief Technology Officer with the Institute of Electronics, Communications and Information Technology (ECIT), QUB. He has authored over 500 scientific papers in major journals and referred international conferences, and two textbooks. He holds patents related to self-tracking antennas and has contributed invited papers and book chapters. His current research interests include physical layer secure active antenna techniques. In 2012, he was awarded the IET Senior Achievement Award, the Mountbatten Medal. He is fellow of the Royal Academy of Engineering.